ANNUAL REVIEWS

Annual Review of Marine Science

The Bottom Boundary Layer

John H. Trowbridge[1] and Steven J. Lentz[2]

[1]Department of Applied Ocean Physics and Engineering, Woods Hole Oceanographic Institution, Woods Hole, Massachusetts 02543, USA; email: jtrowbridge@whoi.edu

[2]Department of Physical Oceanography, Woods Hole Oceanographic Institution, Woods Hole, Massachusetts 02543, USA; email: slentz@whoi.edu

ANNUAL REVIEWS Further

Click here to view this article's online features:
• Download figures as PPT slides
• Navigate linked references
• Download citations
• Explore related articles
• Search keywords

Abstract

The oceanic bottom boundary layer extracts energy and momentum from the overlying flow, mediates the fate of near-bottom substances, and generates bedforms that retard the flow and affect benthic processes. The bottom boundary layer is forced by winds, waves, tides, and buoyancy and is influenced by surface waves, internal waves, and stratification by heat, salt, and suspended sediments. This review focuses on the coastal ocean. The main points are that (*a*) classical turbulence concepts and modern turbulence parameterizations provide accurate representations of the structure and turbulent fluxes under conditions in which the underlying assumptions hold, (*b*) modern sensors and analyses enable high-quality direct or near-direct measurements of the turbulent fluxes and dissipation rates, and (*c*) the remaining challenges include the interaction of waves and currents with the erodible seabed, the impact of layer-scale two- and three-dimensional instabilities, and the role of the bottom boundary layer in shelf-slope exchange.

1. INTRODUCTION

The oceanic bottom boundary layer is the part of the water column, typically with a thickness on the order of meters to tens of meters, that is directly affected by the drag of ocean currents on the seafloor (**Figure 1**). This boundary layer is characterized by turbulent eddies that transport mass, heat, and momentum across the streamlines and the density surfaces that are associated with oceanic currents and stratification, and shares characteristics with boundary layers in engineering (e.g., Jiménez 2012) and the atmospheric sciences (e.g., Wyngaard 1992, Mahrt 2014). The bottom
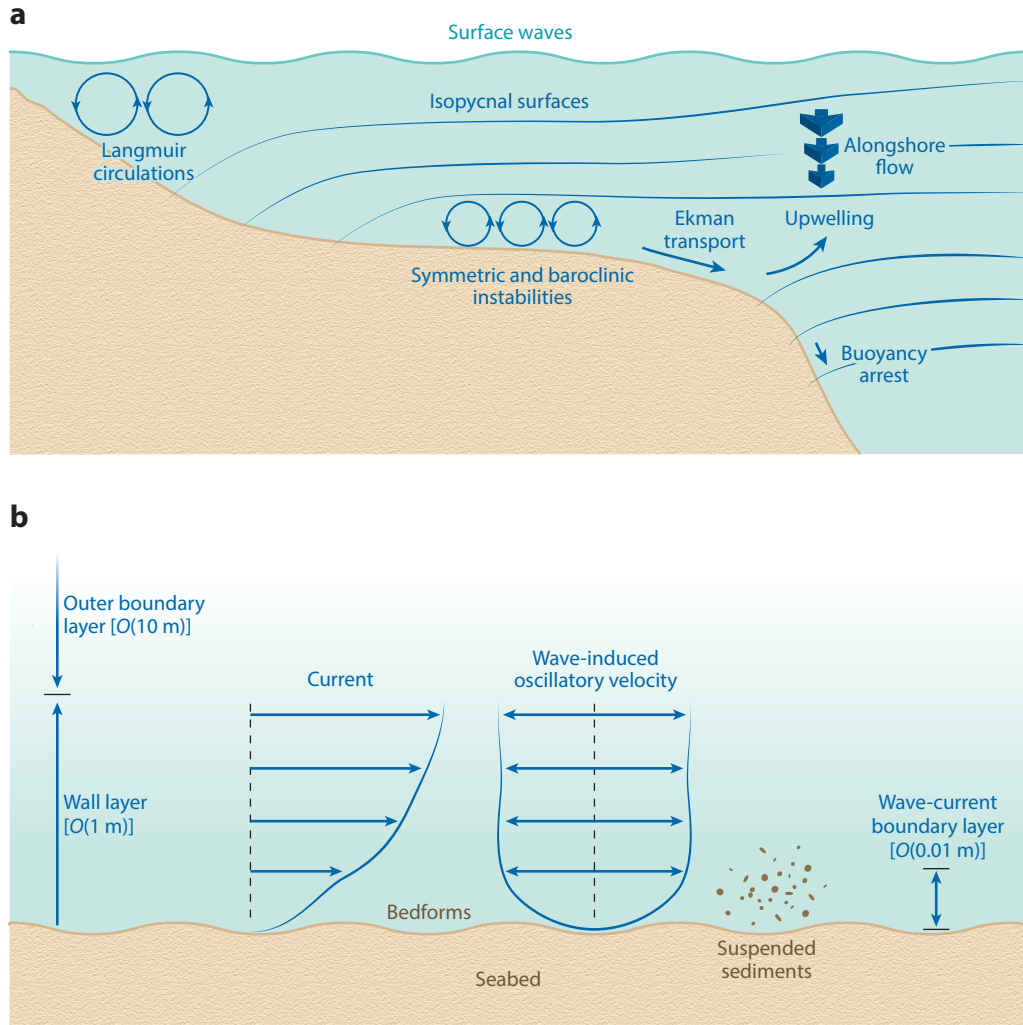
Figure 1

Diagrams of (*a*) selected processes influencing the bottom boundary layer in the coastal ocean and (*b*) the structure of the near-bottom flow.

boundary layer is of intrinsic scientific importance in physical oceanography (e.g., Thorpe 2007) as well as other oceanographic disciplines because it extracts energy and momentum from ocean currents (e.g., McWilliams 2006), provides a mechanism for cross-isobath transport (e.g., Brink 2016), resuspends and transports seafloor sediments (e.g., Dyer & Soulsby 1988), mediates the fate of near-bottom larvae and dissolved substances such as oxygen (e.g., Cowen & Sponaugle 2009), and generates seafloor ripples and dunes (e.g., Charru et al. 2013) that retard the flow and affect benthic biological and chemical processes (e.g., Huettel et al. 2014).

The focus of this review is the bottom boundary layer in the coastal ocean, including estuaries, the surf zone, and the continental shelf. The boundary layer in the coastal ocean is forced by winds, waves, tides, and buoyancy and is influenced by planetary rotation, surface and internal waves, and stratification associated with heat, salt, and suspended sediments. A primary unique feature of the bottom boundary layer in the coastal ocean is the important role played by surface gravity waves, which produce energetic velocity fluctuations that penetrate to the seafloor in sufficiently shallow water.

Previous reviews of the bottom boundary layer in the ocean have focused primarily on the interaction between surface waves and currents that occurs within the centimeters-thick wave-current boundary layer (Grant & Madsen 1986) and the shutdown of the bottom stress that results in theoretical models from the combined effects of stratification, planetary rotation, and a sloping bottom (Garrett et al. 1993). Related reviews have summarized methods for measuring and modeling turbulence in the coastal ocean (Burchard et al. 2008) and described breaking and dissipation mechanisms for internal waves over the continental slope and shelf (Lamb 2014).

The present review summarizes progress and new concepts since the Grant & Madsen (1986) and Garrett et al. (1993) reviews and emphasizes evaluation of physical concepts, derived from theory and simulations, against oceanographic measurements. In the following, we present basic concepts (Section 2), turbulence closure models (Section 3), turbulence measurements (Section 4), wave-current-seabed interaction (Section 5), the outer boundary layer (Section 6), the interaction with the overlying flow (Section 7), and a summary and conclusions (Section 8). Effects of internal waves, reviewed recently by Lamb (2014), are not included.

2. BASIC CONCEPTS

2.1. Mathematical and Conceptual Framework

The mathematical framework is the Reynolds-averaged set of equations for mass, momentum, heat, and salt in the Boussinesq approximation (e.g., Monin & Yaglom 1971, Tennekes & Lumley 1972). Variations of the fluid density are neglected in the fluid mass equation and in the fluid inertia but retained in the gravitational forcing. The Reynolds-averaged motions are resolved, and the unresolved motions are manifested by fluxes of momentum, heat, salt, and sediments, which must be represented in terms of the resolved motions to obtain a closed system of equations.

In the bottom boundary layer, the unresolved fluxes are usually assumed to be dominated by boundary-layer turbulence, and the important fluxes are the turbulent Reynolds shear stress $-\rho_0\overline{u'w'}$, representing the downward transport of streamwise momentum, and the corresponding fluxes of heat, salt, and sediments, combined here for simplicity into the turbulent buoyancy flux $B = (g\rho_0)\overline{\rho'w'}$, representing the upward transport of relatively heavy fluid. The fluxes are often represented in gradient-transport form as $\overline{u'w'} = -K_M\partial U/\partial z$ and $\overline{\rho'w'} = -K_\rho\partial\bar{\rho}/\partial z$. Here, the coordinates are (x, y, z), with x in the streamwise direction (unless otherwise noted) and z vertical and equal to zero at the seafloor; g is the gravitational acceleration; ρ_0 is the constant density that represents the fluid inertia; $\bar{\rho}$ and ρ' are the Reynolds-averaged and turbulent components

of the density, respectively; (U, V, W) and (u', v', w') are the Reynolds-averaged and turbulent components of the velocity, respectively; K_M and K_ρ are the eddy viscosity and diffusivity for momentum and mass, respectively; and overbars denote Reynolds averages. The eddy viscosity and diffusivity are dimensionally and conceptually the product of an intensity and scale that characterize the flux-carrying turbulence. The eddy viscosity and diffusivity are usually similar in magnitude in boundary layers.

The Reynolds-averaged framework assumes the existence of a spectral gap; i.e., the resolved and unresolved scales are assumed to have non-overlapping scales in time and/or space. In observational work in the bottom boundary layer in the coastal ocean, Reynolds averages are usually defined as time averages over 30–60 min, much shorter than the timescales for the variability of the regional-scale currents and stratification (usually on the order of hours to days) but much longer than the timescales of the flux-carrying boundary-layer turbulence (usually on the order of seconds to hundreds of seconds). Measurements in the bottom boundary layer support the existence of a spectral gap in the flux-carrying motions (e.g., Shaw et al. 2001; Trowbridge & Elgar 2001, 2003; Scully et al. 2011), although not always in the horizontal velocity. Surface waves often overlap the turbulence timescales and have important effects in the bottom boundary layer (Sections 4 and 5). Internal waves can occupy the gap between the resolved and unresolved motions and affect the bottom boundary layer (Lamb 2014).

2.2. The Unstratified Wall Layer

The wall layer corresponds to heights z above the bottom that are small in comparison with the boundary-layer thickness δ. In the wall layer, the total shear stress, equal to the sum of the viscous stress $\nu \partial U / \partial z$ and the turbulent Reynolds stress $-\rho_0 \overline{u'w'}$, is approximately equal to the boundary shear stress, denoted τ_b. Under unstratified conditions, the flow locally depends only on z, τ_b, ρ_0, the molecular kinematic viscosity ν, and the characteristics of the boundary roughness, often represented as an equivalent sand roughness, denoted k_s. The primary result is the logarithmic velocity relationship (e.g., Monin & Yaglom 1971, Tennekes & Lumley 1972):

$$\frac{U}{u_*} = \frac{1}{\kappa} \log\left(\frac{z}{z_0}\right).$$
1.

Here, $u_* = \sqrt{\tau_b / \rho_0}$ is the bottom shear velocity; κ is the dimensionless von Kármán constant, with an empirical value near 0.40 (Bailey et al. 2014 and references therein); and z_0 is the boundary roughness length. The equation holds for z/δ much smaller than unity but $z u_* / \nu$ and z/k_s much larger than unity. The roughness length z_0 is an empirical function of k_s, u_*, and ν, proportional to ν/u_* at small $k_s u_* / \nu$ and proportional to k_s at large $k_s u_* / \nu$ (e.g., Jiménez 2004, Allen et al. 2007). In the case of fixed uniformly sized sand, k_s is equal to the sand grain diameter. For other types of roughness, k_s is an empirical function of the roughness scales (Section 5.2).

Although applicable to only a small portion of the boundary layer, Equation 1 is important because it provides a relationship between the near-bottom velocity and the bottom stress, describes $U(z)$ in a region of rapid vertical variation, and provides a framework for parameterizing the viscous and roughness effects that dominate the flow in the immediate vicinity of the boundary. In addition, Equation 1 leads to the model $K_M = \kappa u_* z$, the product of an intensity u_* and scale κz. In spite of seemingly limited applicability, this model often provides a simple but quantitative description of the Reynolds-averaged velocity throughout an unstratified boundary layer (e.g., Madsen 1977, Grant & Madsen 1979). Recent laboratory measurements over a wide range of Reynolds numbers (Bailey et al. 2014 and references therein) support the accuracy of Equation 1
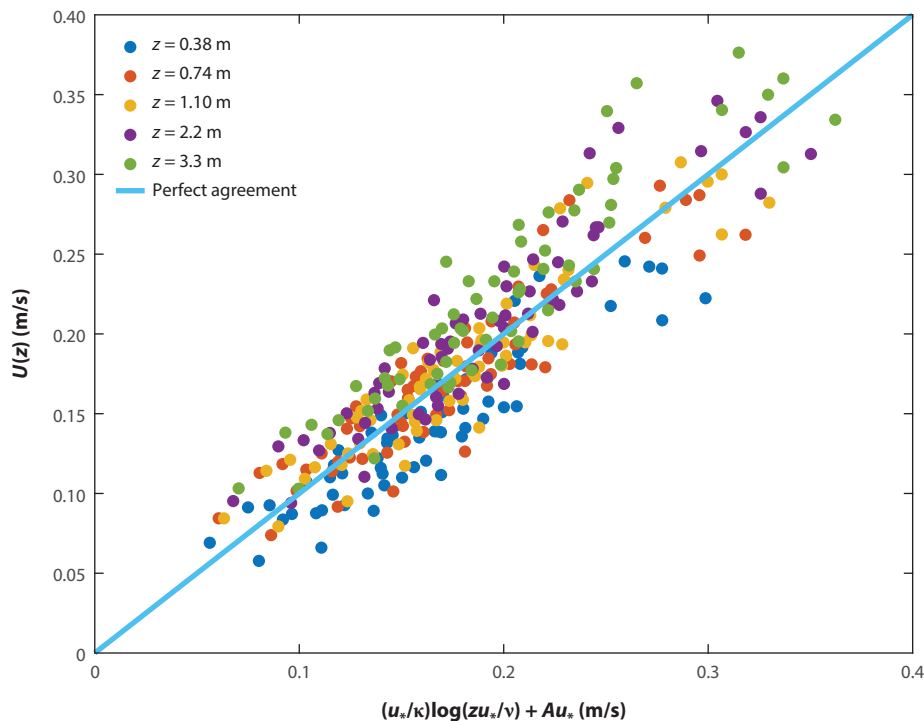
Figure 2

Test of Equation 1 for a smooth boundary against measurements of the Reynolds-averaged velocity and Reynolds stress in weak stratification over a featureless, abiotic, muddy seafloor on the continental shelf south of New England, based on measurements reported by Shaw et al. (2001). Reynolds stresses at each height were computed by direct covariances. Boundary shear stresses were estimated by extrapolating the measured stresses to the seafloor. The measurements are limited to cases in which the array-averaged $z/L < 0.2$, for which the stratification correction to the modeled velocity is less than 10% (see Section 2.3). The abscissa is the modeled value of the Reynolds-averaged velocity based on the measured stresses, with $\kappa = 0.40$ and $A = 5.1$, corresponding to $z_0 = \exp(-\kappa A)\nu/u_* \approx 0.13\nu/u_*$ (e.g., Monin & Yaglom 1971). The ordinate is the measured Reynolds-averaged velocity.

in the unstratified wall layer, and observational tests support its validity in the bottom boundary layer in the ocean (e.g., Sanford & Lien 1999; see also **Figure 2**).

2.3. Effects of Stratification

Although sometimes neutrally or unstably stratified (e.g., Moum et al. 2004), the bottom boundary layer in the ocean is often stably stratified by temperature and salinity (e.g., Trowbridge & Lentz 1998, Lentz & Trowbridge 2001), even within 1 m of the seafloor (Trowbridge & Elgar 2003), and can also be stably stratified by suspended sediment (e.g., Kineke et al. 1996). Stable stratification has a profound effect on boundary-layer turbulence.

Classical investigations have proceeded along three lines. The Miles-Howard theorem, a result of linear stability theory, states that a necessary condition for instability and thus turbulence is that the gradient Richardson number $Ri = N^2/(\partial U/\partial z)^2$, in which $N^2 = -(g/\rho_0)\partial\bar{\rho}/\partial z$ is the squared buoyancy frequency, be less than 1/4 somewhere in the flow (e.g., Drazin & Reid 1981). Measurements and scaling arguments (e.g., Monin & Yaglom 1971, Tennekes & Lumley 1972, Turner

1973) indicate that, even under conditions in which stratification strongly suppresses turbulent mixing, the turbulent kinetic energy equation is often dominated by a balance between the shear production $P = -\overline{u'w'}\partial U/\partial z$, representing the transfer of energy from the Reynolds-averaged flow to the turbulence, and the viscous dissipation rate ε, representing the loss of mechanical energy to heat. The transport terms and buoyancy flux are typically smaller, corresponding to relatively small values of the flux Richardson number $R_f = B/P$. Energetics arguments also establish the Ozmidov scale $L_O = \varepsilon^{1/2}/N^{3/2}$ as an upper bound on the size of the flux-carrying turbulent eddies (e.g., Turner 1973). Dimensional analysis and a long history of measurements in the wall region of the atmospheric surface layer have established Monin-Obukhov similarity theory (e.g., Monin & Yaglom 1971):

$$-\frac{\kappa u_* z}{\overline{u'w'}}\frac{\partial U}{\partial z} = \varphi_M\left(\frac{z}{L}\right)$$ 2.

and

$$-\frac{\kappa u_* z}{\overline{\rho'w'}}\frac{\partial \bar{\rho}}{\partial z} = \varphi_H\left(\frac{z}{L}\right),$$ 3.

which lead to quantitative expressions for the eddy viscosity and diffusivity. Here, $L = u_*^3/(\kappa B)$ is the Monin-Obukhov length and φ_M and φ_H are empirical dimensionless functions that are, with some qualifications (e.g., Mahrt 2014), approximately equal to each other and to $1 + \beta z/L$ in stable stratification, where β is an empirical constant roughly equal to 5 (Businger et al. 1971, Högström 1988, Beljaars & Holtslag 1991, Howell & Sun 1999).

The above results are consistent with Section 2.2 and related to each other. In the limit of weak stratification ($z/L \to 0$), Equation 2 is consistent with Equation 1. The gradient and flux Richardson numbers are equal if $K_M = K_H$. At large stable stratification ($z/L \to +\infty$), Equations 2 and 3 asymptote to a state with $Ri \approx R_f \approx 1/\beta$, similar to the threshold of $Ri = 1/4$ established by linear stability theory. At large stable stratification, with shear production equal to dissipation, the Monin-Obukhov length is proportional to the Ozmidov scale, and the Monin-Obukhov expressions for K_M and K_H are proportional to $u_* L$, again the product of an intensity and scale that characterize the flux-carrying turbulence.

The above results are relevant to the bottom boundary layer in the coastal ocean. Measurements support an approximate balance between shear production and viscous dissipation of turbulent kinetic energy (e.g., Shaw et al. 2001). Estuarine turbulence measurements indicate strong dependence of turbulent mixing on Ri and support the Ozmidov scale as an upper bound on the size of the flux-carrying turbulence (Scully et al. 2011). Although traditionally applied to the wall region of the atmospheric boundary layer, where $\overline{u'w'}$ and B are independent of z, Equations 2 and 3 also apply to conditions in which B varies with z, as in the bottom boundary layer, as shown notably in applications to stratification by suspended sediments (e.g., Monin & Yaglom 1971, Glenn & Grant 1987). Bottom-boundary-layer measurements of the velocity gradient and the fluxes of momentum and buoyancy are consistent with Equations 2 and 3 (**Figure 3**).

2.4. The Energy Cascade and the Energy Spectrum

In the concept of the energy cascade, turbulent velocity fluctuations are generated at a relatively large production scale and subsequently transferred by nonlinear processes to successively smaller scales until they are limited by molecular processes near the much smaller Kolmogorov scale $\eta = (\nu^3/\varepsilon)^{1/4}$. For the idealized case of homogeneous isotropic turbulence, the concept of the energy cascade is quantified in the inertial range, at scales much smaller than the production scale but much larger than the Kolmogorov scale, by the Kolmogorov-Obukhov representation
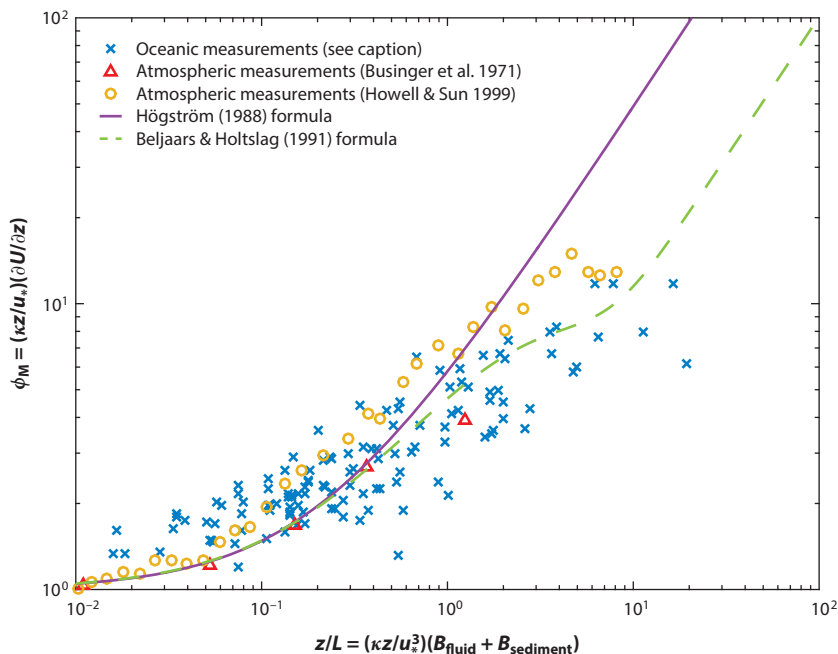
Figure 3

Test of Equation 2 against measurements of the Reynolds-averaged velocity, Reynolds stress, and buoyancy flux in the bottom boundary layer over the continental shelf south of New England, together with atmospheric measurements and empirical formulae. The oceanic values are array averages corresponding to $z = 1.3$ m. For the oceanic measurements, measurements of the three-dimensional velocity vector and the sound speed using acoustic travel-time sensors (Shaw et al. 2001) enabled direct estimates of the Reynolds-averaged velocity gradient and the Reynolds stress, as well as the buoyancy flux B_{fluid} associated with heat and salt. Boundary shear stresses were estimated by extrapolating the measured stresses to the seafloor. Co-located optical measurements of the size distribution of suspended sediments (Agrawal & Traykovski 2001) enabled direct estimates of the buoyancy flux associated with suspended sediments as $B_{sediment} = (g/\rho_0) \sum_n c_n w_{sn} \Delta \rho_n$ (e.g., Monin & Yaglom 1971), where c_n is the measured sediment concentration by volume in the nth size class, and w_{sn} and $\Delta \rho_n$ are the corresponding settling velocity and density anomaly, calculated as a function of particle size using empirical formulae (Sternberg et al. 1999).

of the energy spectrum (e.g., Batchelor 1953, Tennekes & Lumley 1972, Monin & Yaglom 1975):

$$E(k) = \alpha \varepsilon^{2/3} k^{-5/3}. \qquad 4.$$

Here, k is the magnitude of the wave number (k_x, k_y, k_z); $E(k)$ is the kinetic energy spectrum, defined so that $\int_0^{+\infty} E(k) dk$ is the kinetic energy of the turbulence per unit mass of the fluid; and α is the dimensionless Kolmogorov constant, with an empirical value of approximately 1.5 (e.g., McComb 1991, Frisch 1995, Sreenivasan 1995). Corresponding expressions exist for the inertial-range spectra of temperature and salinity fluctuations. Although modified in principle by the intermittency of the small-scale turbulence, Equation 4 remains quantitatively accurate (for a detailed discussion, see, e.g., Frisch 1995). Equation 4 applies to scales much smaller than the production scale even in flows like boundary layers, which are inhomogeneous and anisotropic, because the turbulence at small scales is approximately independent of the details of its origin and thus is locally homogeneous and isotropic.

In typical applications to turbulent boundary layers, one obtains time-series measurements of the velocity at a fixed position; assumes that the turbulence is frozen, so that the time series can be interpreted as one-dimensional spatial series using the mapping $x = Ut$; and computes the one-dimensional spectrum of the turbulent velocities as a function of the streamwise wave number k_x, which is relatable for isotropic turbulence to the spectrum $E(k)$ in Equation 4 (e.g., Tennekes & Lumley 1972, Monin & Yaglom 1975). This procedure, which provides a method for testing the applicability of Equation 4 and obtaining indirect estimates of the dissipation rate, has been applied successfully to the bottom boundary layer in the coastal ocean (e.g., Gross & Nowell 1985, Trowbridge et al. 1999, Lien & Sanford 2004).

3. TURBULENCE CLOSURE MODELS

Equations 1–3 provide the basic elements of a model of the bottom boundary layer: a drag law, i.e., a relationship between the near-bottom velocity and the bottom stress, and a turbulence closure, i.e., a relationship between the turbulent fluxes and the vertical gradients of momentum and buoyancy. More complex turbulence models build on Equations 1–3, and their credibility relies in large part on consistency with these relationships.

The K profile parameterization (Large et al. 1994, Large & Gent 1999, McWilliams & Sullivan 2001, Smyth et al. 2002) generalizes Equations 2 and 3 throughout the boundary layer and incorporates nonlocal mixing, including effects of Langmuir circulations. Although this model is applied primarily to the oceanic and atmospheric surface layers, Wijesekera et al. (2003) applied it to the entire water column, including the bottom boundary layer, in idealized simulations of upwelling and downwelling over the Oregon shelf, finding consistency with simulations based on other turbulence closure models.

An alternative approach, widely used in regional-scale simulations and reviewed in detail by Burchard (2002) and Burchard et al. (2008), is based on the evolution equations, derived from the Navier-Stokes equations, for the turbulent second moments $\overline{u'u'}$, $\overline{u'v'}$, $\overline{u'w'}$, etc. These equations contain higher-order moments that must be parameterized to produce a closed mathematical system. Simplifications lead to gradient-transport relationships, with K_M and K_H dependent on the turbulent kinetic energy, P, ε, $\partial U/\partial z$, and N^2. These are complemented by a parameterized transport equation for the turbulent kinetic energy, together with a second parameterized equation that determines the energy-containing length scale, often the equation for the dissipation rate. The framework is systematic but requires substantial empirical input to determine the multiple dimensionless constants. The approach was substantially improved for marine applications during the 1990s (e.g., Burchard et al. 2008).

In the context of the bottom boundary layer, some of the best tests of the second-moment turbulence closures are in estuaries, where strong forcing, strong stratification, and relatively complete knowledge of the boundary conditions contrast with more complex environments over continental shelves. Tests based on both estuarine-scale simulations, compared with measurements of the Reynolds-averaged velocity and salinity fields (e.g., Warner et al. 2004), and local computations, based on direct measurements of the turbulent fluxes and dissipation rates (Scully et al. 2011), indicate favorable agreement between model computations based on second-moment closures and measurements. In the bottom boundary layer, this success rests in large part on consistency with classical concepts (Section 2).

4. TURBULENCE MEASUREMENTS

Equation 4 and its corollaries provide a means of conceptualizing the turbulence energetics and designing and interpreting turbulence measurements. In the Reynolds-averaged framework, the

turbulence statistics of primary interest in the bottom boundary layer are the turbulent Reynolds shear stress; the corresponding turbulent fluxes of heat, salt, and suspended sediment; the energy dissipation rate; and the corresponding dissipation rates for the temperature and salinity variances.

Modern sensors and analyses, reviewed by Burchard et al. (2008), provide direct measurements or indirect estimates of many of these quantities. Acoustic Doppler velocimeters produce point measurements of velocity with spatial and temporal resolution sufficient to produce direct measurements of the Reynolds stress and indirect inertial-range estimates of the dissipation rate under many conditions. Fast-response temperature and conductivity sensors, co-located with velocity sensors, produce corresponding measurements of the turbulent fluxes of heat and salt and estimates of the dissipation rates for temperature and salinity variance. Acoustic Doppler current profilers produce profiles of the turbulent Reynolds shear stress through the variance method (Stacey et al. 1999). Doppler sonars, which provide range-gated velocity measurements along acoustic beams, enable direct computation of inertial-range wave-number spectra and estimation of the dissipation rate (e.g., Veron & Melville 1999, Gemmrich & Farmer 2004) without the frozen-turbulence approximation. Similarly, seagoing particle-image velocimetry produces two-dimensional maps of the two-dimensional velocity (Nimmo Smith et al. 2002, Luznik et al. 2007, Hackett et al. 2009, Nayak et al. 2015), which can be used to estimate the spatial statistics of the turbulence directly.

Successful application of these methods requires resolution of the appropriate scales. Guidance is provided by atmospheric measurements of auto-spectra and cross-spectra of the three components of the turbulent velocity and the fluctuations of temperature (Kaimal et al. 1972). For example, the Kaimal et al. (1972) expressions for the cospectrum of u' and w', corresponding to Equation 4, show that successful measurement of $\overline{u'w'}$ requires resolution of the k_x between approximately 0.1 and 10 times the dominant flux-carrying scale, equal to z in the unstratified wall layer and limited by the Ozmidov scale in the presence of stable stratification. Measurements across this broad range of scales can place severe constraints on some of the sensors and analyses. For example, acoustic Doppler current profilers often do not resolve small enough scales for successful application of the variance method in strong stable stratification, and the field of view of particle-image velocimetry is sometimes not large enough to resolve the largest stress-carrying scales.

Surface waves, which often overlap in frequency with the flux-carrying turbulence scales in measurements obtained by point sensors, produce special complications. Advection of the turbulence by the wave velocities distorts the observed frequency spectrum, complicating the interpretation of turbulence measurements. Lumley & Terray (1983) modeled this effect using an isotropic model of the underlying spatial turbulence spectrum. Terray et al. (1996), Trowbridge & Elgar (2003), Feddersen et al. (2007), Gerbi et al. (2009), Scully et al. (2016), and others have used the Lumley & Terray (1983) model to produce inertial-range estimates of the dissipation rate in the presence of surface waves. Rosman & Gerbi (2017) used computations based on this model to illustrate effects of surface waves on measurements of turbulent Reynolds stresses.

In addition, the velocity variances associated with surface waves can be orders of magnitude larger than the turbulent velocity variances, which makes extraction of the relatively small turbulence contribution difficult, particularly in the presence of even small uncertainties in the orientation of the velocity sensor with respect to the waves. Trowbridge (1998) proposed mitigation of this effect by differencing measurements obtained by two sensors, separated by a distance larger than the correlation scale of the turbulence but much smaller than the surface wavelength. If the sensor separation is chosen properly, then $(1/2)\overline{\Delta u \Delta w}$, where Δ denotes a velocity difference, is
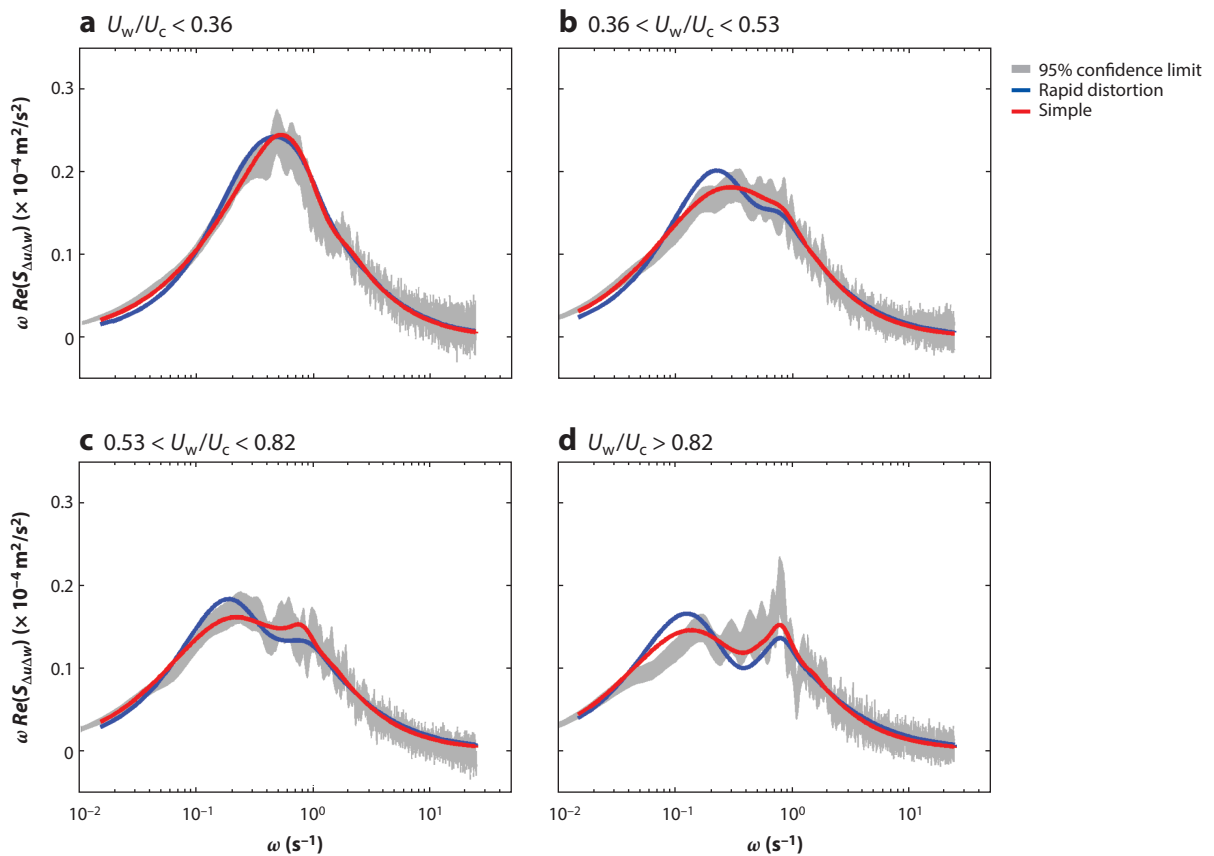
Figure 4

Comparison of measured and modeled cospectra of the stress-carrying turbulence near the seafloor in the presence of surface waves. U_w is the standard deviation of the wave-induced velocity, U_c is the magnitude of the steady current, ω is the radian frequency, and $S_{\Delta u \Delta w}$ is the frequency cross-spectrum of the velocity differences Δu and Δw. The red and blue lines show calculations based on two variants of the model, and the gray shaded region indicates 95% confidence limits for the measurements. Adapted from Trowbridge et al. (2017).

an approximately wave-free measurement of $\overline{u'w'}$. Shaw & Trowbridge (2001) and Feddersen & Williams (2007) proposed extensions of this method.

To enable interpretation and assessment of stress measurements obtained by the differencing method, Trowbridge et al. (2017) proposed a model of the cospectrum of Δu and Δw based on the Lumley & Terray (1983) analysis and the rapid-distortion solution for turbulence in mean shear (Townsend 1980). Model computations and measurements over the inner shelf show distortion of the cospectrum in the presence of surface waves and demonstrate that the model captures the main features of the wave effects (**Figure 4**). These results indicate that the turbulent Reynolds shear stress can be interpreted and assessed with confidence in the presence of energetic surface waves. Note, however, that point measurements of stress obtained by these methods are not necessarily representative of spatially averaged stresses in regions with variations in conditions, particularly seafloor roughness, over short spatial scales.

5. WAVE-CURRENT-SEABED INTERACTION

5.1. The Wave-Current Boundary Layer

In the present review, the primary objective of understanding the wave-current-seabed interaction is to quantify the Reynolds-averaged boundary shear stress, representing the seafloor drag on Reynolds-averaged currents. The boundary shear stress is often expressed by a quadratic drag law:

$$(\tau_{bx}, \tau_{by}) = c_d \rho_0 \sqrt{U^2 + V^2} \, (U, V) \qquad 5.$$

or, alternatively,

$$(\tau_{bx}, \tau_{by}) = c_d' \overline{\sqrt{(U + \tilde{u})^2 + (V + \tilde{v})^2} \, (U + \tilde{u}, V + \tilde{v})}. \qquad 6.$$

Here, τ_{bx} and τ_{by} are the x and y components of the boundary shear stress; tildes denote velocities associated with surface waves; and c_d and c_d' are drag coefficients, which are identical in the absence of waves but different in the presence of waves and are dependent on the heights above bottom at which U and V are calculated or measured, the boundary roughness, the molecular viscosity, and the near-bottom stratification by heat, salt, and suspended sediments. The behavior of c_d' has not been explored in detail theoretically. Observational estimates of c_d' using alongshore momentum balances indicate a threefold difference between values within and just seaward of the surf zone (Feddersen et al. 2004) and no consistent dependence on bedform scale (Feddersen et al. 2003), for reasons that have not been explained. Substantially more work has been devoted to understanding c_d in Equation 5.

A conceptual starting point is the wave-current boundary layer, a centimeters-thick layer just above the seafloor where the current is retarded by energetic turbulence generated by highly sheared oscillatory velocities driven by ocean surface waves (**Figure 1**). Grant & Madsen (1979, 1986) proposed a one-dimensional time-dependent model that predicts a wave-current boundary-layer thickness of u_{*cw}/ω and a two-part logarithmic structure, in which the velocity gradient is reduced relative to Equation 1 within the wave-current boundary layer and the roughness appears to be enhanced relative to Equation 1 above the layer, corresponding to enhancement of the drag coefficient c_d. Soulsby et al. (1993) reported 21 extensions of this model, and many more have been proposed since. Notably, Glenn & Grant (1987) and Styles & Glenn (2000) incorporated stratification by suspended sediments, Davies et al. (1988) and Mellor (2002) reported time-dependent one-dimensional simulations based on second-moment turbulence closure models, and Davies & Villaret (2002) proposed a parameterization of flow separation over large roughness elements.

Measurements within the oscillatory wave-current boundary layer indicate consistency with the one-dimensional Grant & Madsen (1979, 1986) and similar models if, as assumed implicitly in the model formulation, the boundary roughness is small in comparison with the wave-current boundary-layer thickness. In particular, field measurements over fine sands using laser Doppler velocimetry (Trowbridge & Agrawal 1995) indicate an oscillatory turbulent boundary layer with the scales and structure indicated by the one-dimensional models. Similarly, laboratory measurements using acoustic Doppler velocimetry over fixed sand and gravel beds (Hay et al. 2012a,b), and in some cases over rippled erodible beds (Hay et al. 2012c), indicate approximate consistency with statistically one-dimensional dynamics and models. Particle-image velocimetry in an oscillating water tunnel over fixed, uniform, relatively small-scale roughness under strong steady and oscillatory forcing (Yuan & Madsen 2015) clearly shows the two-part logarithmic mean velocity profile predicted by Grant & Madsen (1979, 1986) and quantitative consistency with a slightly revised version of the model.

However, the flow within the oscillatory boundary layer is more complicated if the roughness is larger, particularly if the seabed is erodible. Field measurements over a bed with large ripples using laser Doppler velocimetry indicate complex eddies associated with flow over the ripple crests (Agrawal & Aubrey 1992). Detailed field measurements with vertical arrays of hot-film sensors indicate complexity associated with the rapidly evolving seabed (Foster et al. 2000) and highly intermittent turbulence (Foster et al. 2006). Particle-image velocimetry measurements over steep ripples indicate vortices near ripple crests near times of flow reversal, which penetrate far upward into the flow (Nichols & Foster 2007, Van der Werf et al. 2007). Direct numerical simulations similarly indicate complex three-dimensional structures in oscillatory flow over steep ripples (e.g., Scandura et al. 2000, Blondeaux et al. 2004). Particle-image velocimetry (Nayak et al. 2015) and direct numerical simulations (Ghodke & Apte 2016) also similarly indicate complexity near relatively large roughness elements. The physics and implications of these detailed measurements and simulations have not yet been incorporated conceptually or mathematically into models that can be applied at the regional oceanographic scales of interest, except empirically through the dependence of the model parameter z_0 on the roughness geometry.

5.2. The Bottom Roughness

Application of the Grant & Madsen (1979, 1986) and similar models of the wave-current boundary layer requires specification of the hydrodynamic roughness length z_0. For uniform fixed sand, the dependence of z_0 on the grain diameter, the fluid viscosity, and the shear velocity is well established empirically (e.g., Monin & Yaglom 1971, Schlichting & Gersten 2000). However, determination of z_0 is difficult if the boundary is more complicated, for example, if it is erodible, characterized by relict roughness left by strong flows, dominated by biogenic roughness, or occupying a wide range of roughness scales. This problem is not unique to the coastal ocean: An established general relationship between the physical characteristics of the boundary and the hydrodynamic roughness parameter z_0 does not exist for geophysical flows.

However, substantial progress has been made on quantifying the scales and the hydrodynamic effects of ripples formed by surface waves in well-sorted sands, a common case on continental shelves. Wave-formed ripples assume a variety of configurations, including, in one classification (Hay & Mudge 2005, Hay 2011), irregular ripples, cross-ripples, linear transition ripples, lunate megaripples, and a flat bed. A widely used relationship between the roughness parameter and the dominant ripple wavelength λ and height η is $z_0 \propto \eta^2/\lambda$ (e.g., Grant & Madsen 1982, Nielsen 1992), with a proportionality constant in the range of 0.3–3 (Soulsby 1997), sometimes with a dependence on the angle between the current and the ripple crests (e.g., Drake et al. 1992). Thus, the problem of determining z_0 for wave-formed sand ripples reduces, with some uncertainty, to determination of η, λ, and the ripple orientation.

Some researchers have attempted dynamically based approaches to predicting the scales of wave-formed sand ripples (e.g., Nienhuis et al. 2014), and some have measured the flow over evolving ripples to elucidate the processes that determine the scales (e.g., Nichols & Foster 2009), but most have adopted empirical relationships. According to a widely used empirical scheme for ripples in equilibrium with the forcing (Clifton 1976, Clifton & Dingler 1984, Wiberg & Harris 1994), orbital ripples with $\lambda \propto d$ and $\eta \propto \lambda$ occur for d/D_{50} smaller than a threshold, anorbital ripples with $\lambda \propto D_{50}$ occur for d/D_{50} larger than a greater threshold, and suborbital ripples are a transitional state. Here, d is the wave-induced near-bottom orbital diameter and D_{50} is the median sediment diameter. A recent compilation of laboratory and field measurements under a wide range of conditions indicates the success of this scheme and establishes an empirical relationship for the length and height of equilibrium ripples in fine to medium sand (Nelson et al. 2013).

However, some measurements indicate different behavior in coarse sands, and other measurements indicate significant departures of ripple geometries from equilibrium scales in response to transient forcing by evolving wave conditions. Traykovski (2007) and Ruessink et al. (2015) showed that as the wave orbital diameter d increases, the transition from orbital to suborbital and anorbital ripples is delayed, relative to predictions based on empirical relationships established in finer sediment, for D_{50} greater than roughly 400 μm. A nonequilibrium transient response of ripple dimensions and orientation to time-varying wave conditions has been observed and attributed to physical processes (Traykovski 2007, Maier & Hay 2009) and biological reworking (Hay 2008). Parameterized models of the transient response (Traykovski 2007, Soulsby et al. 2012) capture some, but certainly not all, of the observed temporal variability. Thus, the processes that form ripples and determine their scales are not understood, and the empirical quantification of ripple dimensions in terms of the wave statistics is uncertain, particularly for relatively coarse sand in evolving wave conditions.

5.3. Measurements of the Bottom Drag Coefficient

Recent direct-covariance measurements determine the turbulent Reynolds shear stress above the wave-current boundary layer over an erodible seabed on the inner shelf in the presence of surface waves, accompanied by measurements of the wave and current conditions and the bedform dimensions (Scully et al. 2018). These measurements indicate an order-of-magnitude increase in c_d as the ratio of the wave-induced velocity to the current increases from small to large values (**Figure 5**). The measurements also indicate approximate consistency with the Grant & Madsen (1979, 1986) model, provided that all of the effects described above—i.e., the ripple height and steepness, the angle between the surface waves and the current, and the transient response of the ripples to changes in the wave forcing—are included.

5.4. The Steady Streaming

A phenomenon related to the wave-current boundary layer is the steady streaming, in which friction within the thin oscillatory wave boundary layer produces a wave-induced Reynolds stress, which drives a wave-averaged current (Longuet-Higgins 1953). In laminar flow, the steady streaming driven by progressive waves is in the direction of wave propagation, but simplified models and laboratory measurements have shown streaming in the opposite direction if the oscillatory boundary layer is turbulent and the waves are sufficiently long (Jacobs 1984, Trowbridge & Madsen 1984). The steady streaming is on the order of the wave-induced velocity variance divided by the phase speed and is therefore much weaker than typical alongshore currents driven by winds, waves, tides, and buoyancy. The steady streaming has not been resolved definitively in field measurements, although simulations (Henderson et al. 2004, Uchiyama et al. 2010) indicate better agreement with measurements of the cross-isobath current over a barred beach if the steady streaming is included.

Zou et al. (2006 and references therein) proposed and tested a model of the wave-induced Reynolds stress that forces the steady streaming. The model incorporates the frictional effect within the oscillatory bottom boundary layer (Longuet-Higgins 1953); the sloping seafloor, which modifies the wave-induced vertical velocity because of the condition of zero velocity normal to the boundary; and the dissipative effect of wave breaking near the ocean surface. The model indicates a distinct vertical structure associated with each effect. Oceanic measurements of the wave-induced Reynolds stress are in favorable agreement with model computations, particularly
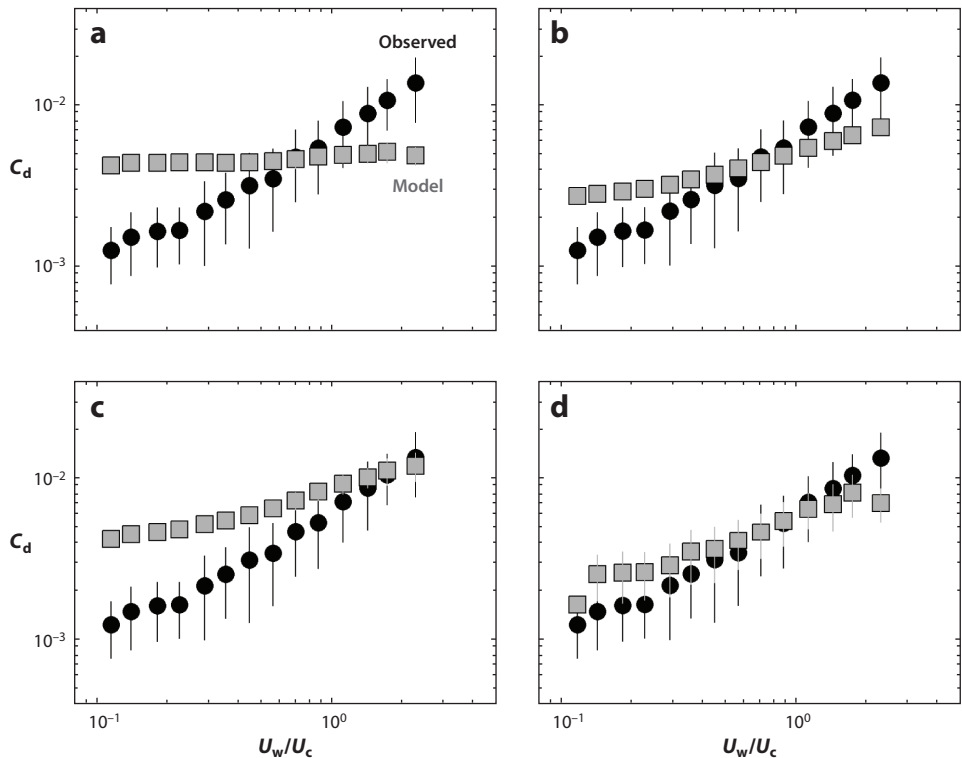
Figure 5

Bottom drag coefficient c_d as a function of the ratio of the standard deviation U_w of the near-bottom wave-induced velocity to the mean velocity U_c. The observed drag coefficients (*black circles*), based on direct-covariance measurements, are compared with model calculations (*gray squares*) using (*a*) only the observed bed roughness, (*b*) the Grant & Madsen (1979) (GM) model using a constant bed roughness, (*c*) the GM model using the observed physical roughness, and (*d*) the GM model using the observed bed roughness and accounting for the orientation of the current relative to the sand ripples. Vertical lines indicate ± 1 standard deviation. Adapted from Scully et al. (2018).

over a steeply sloping seafloor (Wilson et al. 2014 and references therein), for which the second effect is pronounced.

6. THE OUTER BOUNDARY LAYER

Theoretical models and simulations of unstratified and stratified steady and oscillatory turbulent boundary layers over a horizontal seafloor indicate Ekman veering in the presence of planetary rotation as well as a phase shift, relative to the overlying flow, in the presence of unsteady forcing. The thicknesses of unstratified Ekman and oscillatory boundary layers are of order u_*/f and u_*/ω, respectively, where f is the Coriolis parameter and ω is the dominant radian frequency of the oscillatory forcing. Stable stratification suppresses vertical mixing and the boundary-layer thickness and changes the vertical structure of the boundary layer. In particular, stratification with initial uniform buoyancy frequency N suppresses the Ekman-layer thickness, ultimately limiting it to order $u_*/\sqrt{fN}$ for $N \gg f$ (Weatherly & Martin 1978). These behaviors are captured by both

simple turbulence models based on Equations 1–3 and simulations based on more sophisticated second-moment turbulence closures (e.g., Burchard et al. 2008).

Advection, usually not captured by models and simulations of flows over horizontal seafloors, can have a profound effect, not only on the evolution of the density field, but also on the thickness and structure of the boundary layer. The effects of advection are illustrated by the flow of an initially uniformly stratified fluid over a sloping, nonconducting seafloor, which incorporates cross-isobath advection of density anomalies despite being mathematically one-dimensional. Early work (Thorpe 1987 and references therein) focused on the steady case in the absence of a separately forced ambient current, in which satisfaction of the seafloor conditions sets up buoyancy forces that drive a flow. Subsequent work (Garrett et al. 1993 and references therein) addressed the transient forced problem, focusing on the role of buoyancy forces that oppose the externally imposed forcing, which ultimately lead to a state with no bottom stress and no Ekman transport within the bottom boundary layer, termed shutdown, the arrested Ekman layer, or buoyancy arrest. In a comprehensive study of the transient forced case, Brink & Lentz (2010) demonstrated mixing on a timescale of f^{-1} to a thickness of order $u_*/\sqrt{fN}$, followed by transition to shutdown without further thickening in the upwelling case, as opposed to slower evolution to shutdown and a much greater boundary-layer thickness of order $fV_I/(\alpha_s N^2)$ in the downwelling case, with details dependent on the slope Burger number $\alpha_s N/f$. Here, V_I is the interior along-isobath velocity and α_s is the bottom slope.

Theory and simulations indicate that the flow in two or three dimensions is more complicated than indicated by the one-dimensional analyses. Two-dimensional (along-isobath uniform) simulations of wind-driven downwelling over a sloping shelf indicate counter-rotating cells in the bottom boundary layer with vertical scales of tens of meters and cross-isobath scales of kilometers (Allen & Newberger 1996, Zhang et al. 2011). Subsequent theory showed that the inviscid arrested Ekman layer is linearly unstable to symmetric (alongshore-uniform) disturbances with periodic cross-isobath structure at a threshold potential vorticity of zero, and nonlinear two-dimensional simulations indicated counter-rotating cells that tend to drive the potential vorticity toward zero (Allen & Newberger 1998). However, three-dimensional simulations of the bottom boundary layer near a front, while indicating alongshore-uniform instability at relatively small times after initiation of the motion, also indicate the dominance of three-dimensional baroclinic instability at larger times (Brink 2012, 2013; Brink & Cherian 2013).

Observations support some but not all of the results of theory and simulations. Weatherly & Martin (1978) demonstrated cooling and warming resulting from upslope or downslope Ekman transport in the bottom boundary layer. Lentz & Trowbridge (1991) documented thin bottom boundary layers during upwelling and thick layers during downwelling. Trowbridge & Lentz (1998) and Lentz & Trowbridge (2001) showed that the cross-isobath buoyancy force is a dominant term in the cross-isobath momentum balance, consistent with buoyancy arrest, although shutdown was not observed. Stahr & Sanford (1999) did not observe shutdown in the deep western boundary current over the Blake Outer Ridge, possibly because of symmetric or baroclinic instability, as well as other effects that are neglected in the one-dimensional models, including along-isobath density gradients (Trowbridge & Lentz 1998, Lentz & Trowbridge 2001), the finite width of the along-isobath current (Chapman 2002, Chapman & Lentz 2005), topography more complicated than the uniform slope adopted in the models, and secondary circulations that could homogenize the bottom boundary layer under the current (Stahr & Sanford 1999).

Measurements over the inner shelf have indicated energetic near-bottom motions produced by Langmuir cells generated by near-surface wave-current interaction (Gargett et al. 2004, Gargett & Wells 2007). Observations and simulations suggest that crosswind shear associated with the bottom boundary layer in tidal currents can disrupt and distort Langmuir circulations in shallow

water (Kukulka et al. 2011). Large-eddy simulations suggest that Langmuir circulations might disrupt the near-bottom flow and influence the log layer and thus the bottom drag law (Tejada-Martinez et al. 2012). A quantitative observational evaluation of the role of Langmuir circulations in influencing the structure of the bottom boundary layer has not been undertaken.

7. THE INTERACTION WITH THE OVERLYING FLOW

7.1. Vorticity Generation by Spatial Gradients in Bottom Stress and Water Depth

The torque imparted to the water column by the bottom stress in coastal regions with nonuniform bathymetry has an important effect on both the generation and the damping of the vertical vorticity that characterizes eddies over the inner shelf (Signell & Geyer 1991 and references therein). These eddies are resolved by radar measurements of surface currents and simulations (e.g., Ganju et al. 2011, Kirincich et al. 2013, Kirincich 2016), have horizontal scales of kilometers and velocities comparable to those of alongshore wind-driven and tidal currents, and have been hypothesized to play an important role in the transport of heat, salt, and waterborne substances such as larvae, sediments, and pollutants between the inner shelf and midshelf (e.g., Rypina et al. 2011).

The effect of the bottom stress on eddies can be illustrated by the potential vorticity equation in the shallow-water approximation for a constant-density fluid (e.g., Signell & Geyer 1991):

$$\frac{D\varsigma}{Dt} - \frac{f + \varsigma}{H}\frac{DH}{Dt} = \frac{\partial}{\partial y}\left(\frac{\tau_{bx}}{\rho_0 H}\right) - \frac{\partial}{\partial x}\left(\frac{\tau_{by}}{\rho_0 H}\right). \qquad 7.$$

Here, D/Dt is the material derivative, ς is the depth-averaged relative vertical vorticity, H is the water depth, and the right side is the vorticity source produced by the bottom stress. For illustration, the quantities in Equation 7 are estimated from radar measurements of surface currents over the inner shelf south of Martha's Vineyard, Massachusetts (Kirincich et al. 2013, Kirincich 2016), by assuming that the surface currents are representative of the entire depth and, for simplicity, assuming a uniform current outside of the measurement area and assigning a bottom drag coefficient based on the Grant & Madsen (1979) model with uniform bottom roughness and representative time-independent but depth-varying wave conditions.

The measured vorticity for a representative 10-day period is positive inshore of a depth of 20 m, negative offshore of 20 m, and similar in magnitude to the planetary vorticity (**Figure 6a**). The inshore positive vorticity is strongly modulated by the tide, with the onshore positive vorticity generated during flow toward the west. By contrast, the offshore negative vorticity varies at subtidal timescales and appears to be generated by subtidal flows toward the west-northwest. The source region for the vorticity is a shoal (**Figure 6b**), consistent with the measured vorticity in the high-frequency radar measurement area (**Figure 6a**). The spatially variable drag coefficient, which is sensitive to the details of the bedforms and the near-bottom flow (Section 5.3), contributes significantly to the vorticity source.

7.2. Fronts and the Shelf Break

A number of researchers have used two-dimensional (alongshore uniform) simulations to explore detachment or entrainment of the bottom boundary layer near a front or near a shelf break. The underlying concept is that variations in the bottom slope or stratification create gradients in the buoyancy arrest that lead to divergences of the Ekman transport. Romanou & Weatherly (2001) simulated the turbulent Ekman layer over a sloping seafloor in the presence of variable stratification. Their results indicate convergence near the front and export of fluid from the
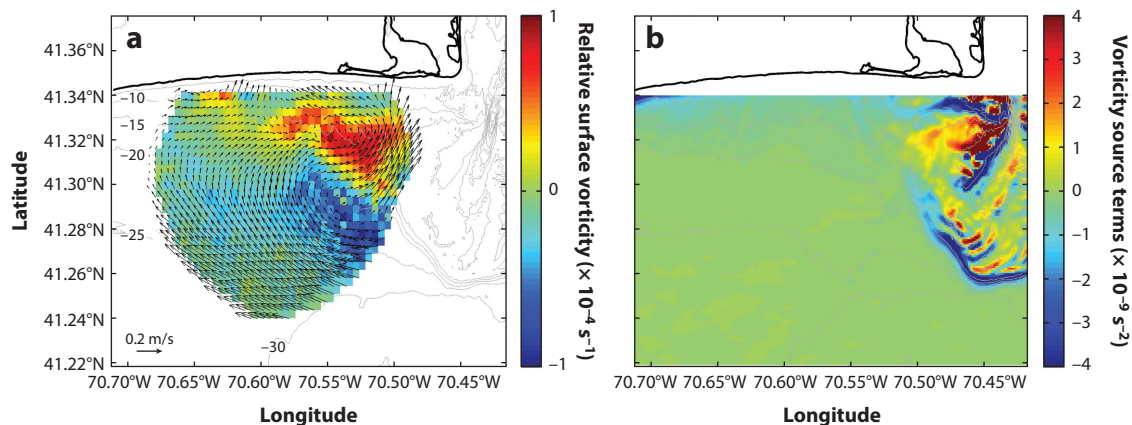
Figure 6

Measurements and model calculations for a region south of Martha's Vineyard, Massachusetts, including (*a*) mean surface velocity (*arrows*) and relative surface vorticity (*color scale*) for the period July 20–August 1, 2011, based on high-frequency radar measurements of surface currents (data courtesy of A. Kirincich, Woods Hole Oceanographic Institution), and (*b*) vorticity source terms (the right side of Equation 7) based on an assumed spatially uniform current of 0.1 m/s toward the west and a bottom drag coefficient following Grant & Madsen (1979) for a wave height of 2 m, a wave period of 8 s, wave-induced near-bottom velocity determined from linear wave theory using the local depth, and a uniform roughness length of 1.7×10^{-5} m. Depth contours are in meters.

boundary layer in downwelling-favorable interior flow, as opposed to divergence near the front and import of fluid to the boundary layer during upwelling-favorable flow. The numerical results indicate that the position and strength of the convergence and divergence are controlled by the background diffusivity and the strength of the stratification, and that the bottom stress near the front is larger than ambient during downwelling and smaller during upwelling. Zhang et al. (2011) explored the circulation near the New England shelf-break front, finding pronounced seasonal variability and persistent upwelling at the shelf break, with most of the upwelled water from the upper slope, instead of the shelf, in the form of a detached bottom boundary layer. Benthuysen et al. (2015) illustrated upwelling at a shelf-break front in downwelling-favorable along-isobath flow, using an idealized flat shelf and uniform continental slope. In these simulations, buoyancy arrest and ageostrophic upslope flow over the slope retard the offshore Ekman transport, and the convergence in the transport produces upwelling offshore of the shelf break, similar to the results of Zhang et al. (2011). Scaling and numerical simulations support a quantitative expression for the vertical velocity in terms of the Ekman transport over the shelf and the Burger number and boundary-layer thickness over the slope.

Several observational studies have documented upwelling near the shelf break, in qualitative agreement with some of the simulations, with inferred vertical velocities of 5–20 m/day. Houghton & Visbeck (1998) and Houghton et al. (2006) tracked dye injected into the bottom boundary layer. Barth et al. (1998) tracked suspended material from the bottom boundary layer over the shelf as it upwelled into the shelf-break front. Pickart (2000) tracked well-mixed water from the bottom boundary layer on the shelf as it upwelled. Barth et al. (2004) tracked upwelling using an isopycnal float. Whether the upwelling is associated with the break in topography or the associated front separating shelf from slope water is unclear. Consistency with the simulations and scalings has not been established. The role of two-dimensional symmetric instabilities (Allen & Newberger 1998, Zhang et al. 2011) and three-dimensional baroclinic instabilities (Brink 2012, 2013; Brink & Cherian 2013) is not known.

8. SUMMARY AND CONCLUSIONS

This review of the bottom boundary layer in the coastal ocean has addressed basic turbulence concepts, turbulence closure models, turbulence measurements, flow-seabed interaction, the outer boundary layer, and the interaction with the overlying flow. The key points are the following:

- Under conditions in which the underlying assumptions hold, the structure and dynamics of the bottom boundary layer in the coastal ocean are consistent with classical conceptions of boundary-layer turbulence (Section 2) and simulations based on second-moment turbulence closure models (Section 3).
- Modern sensors and analyses produce accurate direct measurements of the turbulent Reynolds stress and buoyancy flux, as well as accurate inertial-range estimates of the dissipation rates for turbulent kinetic energy and for temperature and salinity variance, even under conditions in which surface waves mask the turbulence and distort the turbulence spectra (Section 4).
- The wave-current boundary layer is represented well by existing one-dimensional models when the roughness elements are much smaller than the layer thickness, consistent with the underlying assumptions, but a consistent conceptual and mathematical framework, simple enough to be applied in regional-scale simulations, does not exist for roughness elements that are comparable to or larger than the layer thickness (Section 5).
- The bottom drag coefficient is sensitive to the details of the flow-seabed interaction, including the turbulence dynamics in the wave-current boundary layer, the ripple height and steepness, the angle between the surface waves and the current, and the transient response of the ripples to changes in the wave forcing, particularly in coarse sands (Section 5).
- Some aspects of the buoyancy arrest caused by planetary rotation, stratification, and a sloping bottom are consistent with observations, but simulations indicate important effects of layer-scale two-dimensional symmetric and three-dimensional baroclinic instabilities, which are not well understood in this context and have not been explored or documented observationally (Section 6).
- Simulations suggest that Langmuir circulations can penetrate to the seafloor and disrupt the structure of the near-bottom flow, but this effect has not been explored or documented observationally (Section 6).
- The spatial variability of the bottom stress and the bottom drag coefficient contributes significantly to the generation over the inner shelf of kilometer-scale eddies, which are important in cross-isobath transport of waterborne substances (Section 7).
- Simple conceptions based on buoyancy arrest of the behavior near the shelf break have been studied in idealized simulations, but these have not been explored or documented observationally, and the role of the bottom boundary layer in shelf-slope exchange is not understood (Section 7).

Thus, the remaining challenges include the interaction of waves and currents with the erodible seabed, particularly in the presence of coarse sediments, the impact of layer-scale two- and three-dimensional instabilities, and the role of the bottom boundary layer in shelf-slope exchange.

DISCLOSURE STATEMENT

The authors are not aware of any affiliations, memberships, funding, or financial holdings that might be perceived as affecting the objectivity of this review.

ACKNOWLEDGMENTS

LITERATURE CITED

Agrawal YC, Aubrey DG. 1992. Velocity observations above a rippled bed using laser Doppler velocimetry. *J. Geophys. Res.* 97:20249–59

Agrawal YC, Traykovski P. 2001. Particles in the bottom boundary layer: concentration and size dynamics through events. *J. Geophys. Res.* 106:9533–42

Allen JJ, Shockling MA, Kunkel GJ, Smits AJ. 2007. Turbulent flow in smooth and rough pipes. *Philos. Trans. R. Soc. A* 365:699–714

Allen JS, Newberger PA. 1996. Downwelling circulation on the Oregon continental shelf. Part I: response to idealized forcing. *J. Phys. Oceanogr.* 26:2011–35

Allen JS, Newberger PA. 1998. On symmetric instabilities in bottom boundary layers. *J. Phys. Oceanogr.* 28:1131–51

Bailey SCC, Vallikivi M, Hultmark M, Smits AJ. 2014. Estimating the value of von Kármán's constant in turbulent pipe flow. *J. Fluid Mech.* 749:79–98

Barth JA, Bogucki D, Pierce SD, Kosro PM. 1998. Secondary circulation associated with a shelfbreak front. *Geophys. Res. Lett.* 25:2761–64

Barth JA, Hebert D, Dale AC, Ullman DS. 2004. Direct observations of along-isopycnal upwelling and diapycnal velocity at a shelfbreak front. *J. Phys. Oceanogr.* 34:543–65

Batchelor GK. 1953. *The Theory of Homogeneous Turbulence*. New York: Cambridge Univ. Press

Beljaars ACM, Holtslag AAM. 1991. Flux parameterization over land surface for atmospheric models. *J. Appl. Meteorol.* 30:327–41

Benthuysen J, Thomas LN, Lentz SJ. 2015. Rapid generation of upwelling at a shelf break caused by buoyancy shutdown. *J. Phys. Oceanogr.* 45:294–312

Blondeaux P, Scandura P, Vittori G. 2004. Coherent structures in an oscillatory separated flow: numerical experiments. *J. Fluid Mech.* 518:215–29

Brink KH. 2012. Baroclinic instability of an idealized tidal mixing front. *J. Mar. Res.* 70:661–88

Brink KH. 2013. Instability of a tidal mixing front in the presence of realistic tides and mixing. *J. Mar. Res.* 71:227–52

Brink KH. 2016. Cross-shelf exchange. *Annu. Rev. Mar. Sci.* 8:59–78

Brink KH, Cherian DA. 2013. Instability of an idealized tidal mixing front: symmetric instabilities and frictional effects. *J. Mar. Res.* 71:425–50

Brink KH, Lentz SJ. 2010. Buoyancy arrest and bottom Ekman transport. Part I: steady flow. *J. Phys. Oceanogr.* 40:621–35

Burchard H. 2002. *Applied Turbulence Modelling in Marine Waters*. New York: Springer-Verlag

Burchard H, Craig PD, Gemmrich JR, van Haren H, Mathieu PP, et al. 2008. Observational and numerical modeling methods for quantifying coastal ocean turbulence and mixing. *Prog. Oceanogr.* 76:399–42

Businger JA, Wyngaard JC, Izumi Y, Bradley EF. 1971. Flux-profile relationships in the atmospheric surface layer. *J. Atmos. Sci.* 28:181–89

Chapman DC. 2002. Deceleration of a finite-width, stratified current over a sloping bottom: frictional spin-down or buoyancy shutdown? *J. Phys. Oceanogr.* 32:336–52

Chapman DC, Lentz SJ. 2005. Acceleration of a stratified current over a sloping bottom, driven by an alongshelf pressure gradient. *J. Phys. Oceanogr.* 35:1305–17

Charru F, Andreotti B, Claudin P. 2013. Sand ripples and dunes. *Annu. Rev. Fluid Mech.* 45:469–93

Clifton HE. 1976. Wave-formed sedimentary structures: a conceptual model. In *Beach and Nearshore Sedimentation*, ed. RA Davis Jr., RL Ethington, pp. 126–48. SEPM Spec. Publ. 24. Tulsa, OK: Soc. Sediment. Geol.

Clifton HE, Dingler JR. 1984. Wave-formed structures and paleoenvironmental reconstruction. *Mar. Geol.* 60:165–98

Cowen RK, Sponaugle S. 2009. Larval dispersal and marine population connectivity. *Annu. Rev. Mar. Sci.* 1:443–66

Davies AG, Soulsby RL, King HL. 1988. A numerical model of the combined wave and current bottom boundary layer. *J. Geophys. Res.* 93:491–508

Davies AG, Villaret C. 2002. Prediction of sand transport rates by waves and currents in the coastal zone. *Cont. Shelf Res* 22:2725–37

Drake DE, Cacchione DA, Grant WD. 1992. Shear stress and bed roughness estimates for combined wave and current flows over a rippled bed. *J. Geophys. Res.* 97:2319–26

Drazin PG, Reid WH. 1981. *Hydrodynamic Stability*. New York: Cambridge Univ. Press

Dyer KR, Soulsby RL. 1988. Sand transport on the continental shelf. *Annu. Rev. Fluid Mech.* 20:295–324

Feddersen F, Gallagher E, Guza RT, Elgar S. 2003. The drag coefficient, bottom roughness, and wave-breaking in the nearshore. *Coast. Eng.* 48:189–95

Feddersen F, Guza R, Elgar S. 2004. Inverse modeling of one-dimensional setup and alongshore current in the nearshore. *J. Phys. Oceanogr.* 34:920–33

Feddersen F, Trowbridge JH, Williams AJ. 2007. Vertical structure of dissipation in the nearshore. *J. Phys. Oceangr.* 37:1764–77

Feddersen F, Williams AJ. 2007. Direct estimation of the Reynolds stress vertical structure in the nearshore. *J. Atmos. Ocean. Technol.* 24:102–16

Foster DL, Beach RA, Holman RA. 2000. Field observations of the wave bottom boundary layer. *J. Geophys. Res.* 105:19,631–48

Foster DL, Beach RA, Holman RA. 2006. Turbulence observations of the nearshore wave bottom boundary layer. *J. Geophys. Res.* 111:C04011

Frisch U. 1995. *Turbulence: The Legacy of A. N. Kolmogorov*. New York: Cambridge Univ. Press

Ganju NK, Lentz SJ, Kirincich AR, Farrar JT. 2011. Complex mean circulation over the inner shelf south of Martha's Vineyard revealed by observations and a high-resolution model. *J. Geophys. Res.* 116:C10036

Gargett AE, Wells JR. 2007. Langmuir turbulence in shallow water. Part 1. Observations. *J. Fluid Mech.* 576:27–61

Gargett AE, Wells JR, Tejada-Martınez AE, Grosch CE. 2004. Langmuir supercells: a mechanism for sediment resuspension and transport in shallow seas. *Science* 306:1925–28

Garrett C, MacCready P, Rhines P. 1993. Boundary mixing and arrested Ekman layers: rotating stratified flow near a sloping boundary. *Annu. Rev. Fluid Mech.* 25:291–323

Gemmrich JR, Farmer DM. 2004. Near-surface turbulence in the presence of breaking waves. *J. Phys. Oceanogr.* 34:1067–86

Gerbi GP, Trowbridge JH, Terray EA, Plueddemann AJ, Kukulka T. 2009. Observations of turbulence in the ocean surface boundary layer: energetics and transport. *J. Phys. Oceanogr.* 39:1077–96

Ghodke CD, Apte SV. 2016. DNS study of particle-bed-turbulence interactions in an oscillatory wall-bounded flow. *J. Fluid Mech.* 792:232–51

Glenn SM, Grant WD. 1987. A suspended sediment stratification correction for combined wave and current flows. *J. Geophys. Res.* 92:8244–64

Grant WD, Madsen OS. 1979. Combined wave and current interaction with a rough bottom. *J. Geophys. Res.* 84:1797–808

Grant WD, Madsen OS. 1982. Moveable bed roughness in unsteady oscillatory flow. *J. Geophys. Res.* 87:469–81

Grant WD, Madsen OS. 1986. The continental-shelf bottom boundary layer. *Annu. Rev. Fluid Mech.* 18:265–305

Gross TF, Nowell RM. 1985. Spectral scaling in a tidal boundary layer. *J. Phys. Oceanogr.* 15:496–508

Hackett E, Luznik L, Katz J, Osborn TR. 2009. Effect of finite spatial resolution on the turbulent energy spectrum measured in the coastal ocean bottom boundary layer. *J. Atmos. Ocean. Technol.* 26:2610–25

Hay AE. 2008. Near-bed turbulence and relict waveformed sand ripples: observations from the inner shelf. *J. Geophys. Res.* 113:C04040

Hay AE. 2011. Geometric bed roughness and the bed state storm cycle. *J. Geophys. Res.* 116:C04017

Hay AE, Mudge T. 2005. Principal bed states during SandyDuck97: occurrence, spectral anisotropy, and the bed state storm cycle. *J. Geophys. Res.* 110:C03013

Hay AE, Zedel L, Cheel R, Dillon J. 2012a. Observations of the vertical structure of turbulent oscillatory boundary layers above fixed roughness beds using a prototype wideband coherent Doppler profiler: 1. The oscillatory component of the flow. *J. Geophys. Res.* 117:C03005

Hay AE, Zedel L, Cheel R, Dillon J. 2012b. Observations of the vertical structure of turbulent oscillatory boundary layers above fixed roughness using a prototype wideband coherent Doppler profiler: 2. Turbulence and stress. *J. Geophys. Res.* 117:C03006

Hay AE, Zedel L, Cheel R, Dillon J. 2012c. On the vertical and temporal structure of flow and stress within the turbulent oscillatory boundary layer above evolving sand ripples. *Cont. Shelf Res.* 46:31–49

Henderson SM, Allen JS, Newberger PA. 2004. Nearshore sandbar migration predicted by an eddy-diffusive boundary layer model. *J. Geophys. Res.* 109:C06024

Högström U. 1988. Non-dimensional wind and temperature profiles in the atmospheric surface layer: a re-evaluation. *Bound. Layer Meteorol.* 42:55–78

Houghton RW, Hebert D, Prater M. 2006. Circulation and mixing at the New England shelfbreak front: results of purposeful tracer experiments. *Prog. Oceanogr.* 70:289–312

Houghton RW, Visbeck M. 1998. Upwelling and convergence in the Middle Atlantic Bight shelfbreak front. *Geophys. Res. Lett.* 25:2765–68

Howell J, Sun J. 1999. Surface layer fluxes in stable conditions. *Bound. Layer Meteorol.* 90:495–520

Huettel M, Berg P, Kostka JE. 2014. Benthic exchange and biogeochemical cycling in permeable sediments. *Annu. Rev. Mar. Sci.* 6:23–51

Jacobs SJ. 1984. Mass transport in a turbulent boundary layer under a progressive water wave. *J. Fluid Mech.* 146:303–12

Jiménez J. 2004. Turbulent flows over rough walls. *Annu. Rev. Fluid Mech.* 36:173–96

Jiménez J. 2012. Cascades in wall-bounded turbulence. *Annu. Rev. Fluid Mech.* 44:27–45

Kaimal JC, Wyngaard JC, Izumi Y, Coté OR. 1972. Spectral characteristics of surface layer turbulence. *Q. J. R. Meteorol. Soc.* 98:563–89

Kineke GC, Sternberg RW, Trowbridge JH, Geyer WR. 1996. Fluid-mud processes on the Amazon continental shelf. *Cont. Shelf Res.* 16:667–96

Kirincich AR. 2016. The occurrence, drivers, and implications of submesoscale eddies on the Martha's Vineyard inner shelf. *J. Phys. Oceanogr.* 46:2645–62

Kirincich AR, Lentz SJ, Farrar JT. 2013. The spatial structure of tidal and mean circulation over the inner shelf south of Martha's Vineyard, Massachusetts. *J. Phys. Oceanogr.* 43:1940–58

Kukulka T, Plueddemann AJ, Trowbridge JH, Sullivan PP. 2011. The influence of crosswind tidal currents on Langmuir circulation in a shallow ocean. *J. Geophys. Res.* 116:C08005

Lamb KG. 2014. Internal wave breaking and dissipation mechanisms on the continental slope/shelf. *Annu. Rev. Fluid Mech.* 46:231–54

Large WG, Gent PR. 1999. Validation of vertical mixing in an equatorial ocean model using large eddy simulations and observations. *J. Phys. Oceanogr.* 29:449–64

Large WG, McWilliams JC, Doney SC. 1994. Oceanic vertical mixing: a review and a model with nonlocal boundary layer parameterization. *Rev. Geophys.* 32:363–403

Lentz SJ, Trowbridge JH. 1991. The bottom boundary layer over the northern California shelf. *J. Phys. Oceanogr.* 21:1186–201

Lentz SJ, Trowbridge JH. 2001. A dynamical description of fall and winter mean current profiles over the northern California shelf. *J. Phys. Oceangr.* 31:914–31

Lien RC, Sanford TB. 2004. Turbulence spectra and local similarity scaling in a strongly stratified oceanic bottom boundary layer. *Cont. Shelf Res.* 24:375–92

Longuet-Higgins MS. 1953. Mass transport in water waves. *Philos. Trans. R. Soc. Lond. A* 245:535–81

Lumley JL, Terray EA. 1983. Kinematics of turbulence convected by a random wave field. *J. Phys. Oceanogr.* 13:2000–7

Luznik L, Gurka R, Zhu W, Nimmo Smith WAM, Katz J, Osborn TR. 2007. Distributions of energy spectra, Reynolds stresses, turbulence production and dissipation in a tidally driven bottom boundary layer. *J. Phys. Oceanogr.* 37:1527–50

Madsen OS. 1977. A realistic model of the wind-induced Ekman boundary layer. *J. Phys. Oceanogr.* 7:248–55

Mahrt L. 2014. Stably stratified atmospheric boundary layers. *Annu. Rev. Fluid Mech.* 46:23–45

Maier I, Hay AE. 2009. Occurrence and orientation of anorbital ripples in near-shore sands. *J. Geophys. Res.* 114:F04022

McComb WD. 1991. *The Physics of Fluid Turbulence*. Oxford, UK: Oxford Univ. Press

McWilliams JC. 2006. *Fundamentals of Geophysical Fluid Dynamics*. New York: Cambridge Univ. Press

McWilliams JC, Sullivan P. 2001. Vertical mixing by Langmuir circulations. *Spill Sci. Technol. Bull.* 6:225–37

Mellor GL. 2002. Oscillatory bottom boundary layers. *J. Phys. Oceanogr.* 32:3075–88

Monin AS, Yaglom AM. 1971. *Statistical Fluid Mechanics: Mechanics of Turbulence*, *Volume 1*. Mineola, NY: Dover

Monin AS, Yaglom AM. 1975. *Statistical Fluid Mechanics: Mechanics of Turbulence*, *Volume 2*. Mineola, NY: Dover

Moum JN, Perlin A, Klymak JM, Levine MD, Boyd T, Kosro PM. 2004. Convectively-driven mixing in the bottom boundary layer over the continental shelf during downwelling. *J. Phys. Oceanogr.* 34:2189–202

Nayak AR, Li C, Kiani BT, Katz J. 2015. On the wave and current interaction with a rippled seabed in the coastal ocean bottom boundary layer. *J. Geophys. Res.* 120:4595–624

Nelson TR, Voulgaris G, Traykovski P. 2013. Predicting wave-induced ripple equilibrium geometry. *J. Geophys. Res.* 118:3202–20

Nichols CS, Foster DL. 2007. Full-scale observations of wave-induced vortex generation over a rippled bed. *J. Geophys. Res.* 112:C10015

Nichols CS, Foster DL. 2009. Observations of bed form evolution with field-scale oscillatory hydrodynamic forcing. *J. Geophys. Res.* 114:C08010

Nielsen P. 1992. *Coastal Bottom Boundary Layers and Sediment Transport*. New York: World Sci.

Nienhuis JH, Perron JT, Kao JCT, Myrow PM. 2014. Wavelength selection and symmetry breaking in orbital wave ripples. *J. Geophys. Res.* 119:2239–57

Nimmo Smith WAM, Atsavapranee P, Katz J, Osborn T. 2002. PIV measurements in the bottom boundary layer of the coastal ocean. *Exp. Fluids* 33:962–71

Pickart RS. 2000. Bottom boundary layer structure and detachment in the shelfbreak jet of the Middle Atlantic Bight. *J. Phys. Oceanogr.* 30:2668–86

Romanou A, Weatherly GL. 2001. Numerical simulations of buoyant Ekman layers in the presence of variable stratification. Part I: constant interior forcing. *J. Phys. Oceanogr.* 31:3096–120

Rosman JH, Gerbi GP. 2017. Interpreting fixed-location observations of turbulence advected by waves: insights from spectral models. *J. Phys. Oceanogr.* 47:909–31

Ruessink G, Brinkkemper JA, Kleinhans MG. 2015. Geometry of wave-formed orbital ripples in coarse sand. *J. Mar. Sci. Eng.* 3:1568–94

Rypina II, Scott SE, Pratt LJ, Brown MG. 2011. Investigating the connection between complexity of isolated trajectories and Lagrangian coherent structures. *Nonlinear Process. Geophys.* 18:977–87

Sanford TB, Lien RC. 1999. Turbulent properties in a homogeneous tidal bottom boundary layer. *J. Geophys. Res.* 104:1245–57

Scandura P, Vittori G, Blondeaux P. 2000. Three-dimensional oscillatory flow over steep ripples. *J. Fluid Mech.* 412:355–78

Schlichting H, Gersten K. 2000. *Boundary Layer Theory*. New York: Springer-Verlag

Scully ME, Geyer WR, Trowbridge JH. 2011. The influence of stratification and non-local turbulent production on estuarine turbulence: an assessment of turbulence closure with field observations. *J. Phys. Oceanogr.* 41:166–85

Scully ME, Trowbridge JH, Fisher AW. 2016. Observations of the transfer of energy and momentum to the oceanic surface boundary layer beneath breaking waves. *J. Phys. Oceanogr.* 46:1823–37

Scully ME, Trowbridge JH, Sherwood CR. 2018. Direct-covariance measurements of turbulent Reynolds shear stresses over erodible sand beds in the presence of energetic forcing by surface waves. *J. Geophys. Res.* In press

Shaw WJ, Trowbridge JH. 2001. The direct estimation of near-bottom turbulent fluxes in the presence of energetic wave motions. *J. Atmos. Ocean. Technol.* 18:1540–57

Shaw WJ, Trowbridge JH, Williams AJ. 2001. Budgets of turbulent kinetic energy and scalar variance in the continental shelf bottom boundary layer. *J. Geophys. Res.* 106:9551–64

Signell RP, Geyer WR. 1991. Transient eddy formation around headlands. *J. Geophys. Res.* 96:2561–75

Smyth WD, Skyllingstad ED, Crawford GB, Wijesekera H. 2002. Nonlocal fluxes and Stokes drift effects in the K-profile parameterization. *Ocean Dyn.* 52:104–15

Soulsby RL. 1997. *Dynamics of Marine Sands: A Manual for Practical Applications*. London: Telford

Soulsby RL, Hamm L, Klopman G, Myrhaug D, Simons RR, Thomas GP. 1993. Wave-current interaction within and outside the wave-current boundary layer. *Coast. Eng.* 21:41–69

Soulsby RL, Whitehouse RJS, Marten KV. 2012. Prediction of time-evolving sand ripples in shelf seas. *Cont. Shelf Res.* 38:47–62

Sreenivasan KR. 1995. On the universality of the Kolmogorov constant. *Phys. Fluids* 7:2778–84

Stacey MT, Monismith SG, Burau JR. 1999. Measurements of Reynolds stress profiles in unstratified tidal flow. *J. Geophys. Res.* 104:10933–49

Stahr FR, Sanford TB. 1999. Transport and bottom boundary layer observations of the North Atlantic Deep Western Boundary Current at the Blake Outer Ridge. *Deep-Sea Res. II* 46:205–43

Sternberg RW, Berhane I, Ogston AS. 1999. Measurement of size and settling velocity of suspended aggregates on the northern California continental shelf. *Mar. Geol.* 154:43–53

Styles R, Glenn SM. 2000. Modeling stratified wave and current bottom boundary layers on the continental shelf. *J. Geophys. Res.* 105:24119–39

Tejada-Martinez AE, Grosch CE, Sinha N, Akan C, Martinat G. 2012. Disruption of the bottom log layer in large-eddy simulations of full-depth Langmuir circulation. *J. Fluid Mech.* 699:79–93

Tennekes H, Lumley JL. 1972. *A First Course in Turbulence*. Cambridge, MA: MIT Press

Terray EA, Donelan MA, Agrawal YC, Drennan WM, Kahma KK, et al. 1996. Estimates of kinetic energy dissipation under breaking waves. *J. Phys. Oceanogr.* 26:792–807

Thorpe SA. 1987. Current and temperature variability on the continental slope. *Philos. Trans. R. Soc. Lond. A* 323:471–517

Thorpe SA. 2007. *Ocean Turbulence*. New York: Cambridge Univ. Press

Townsend AA. 1980. *The Structure of Turbulent Shear Flow*. New York: Cambridge Univ. Press

Traykovski P. 2007. Observations of wave orbital scale ripples and a nonequilibrium time-dependent model. *J. Geophys. Res.* 112:C06026

Trowbridge JH. 1998. On a technique for measurement of turbulent shear stress in the presence of surface waves. *J. Atmos. Ocean. Technol.* 15:290–98

Trowbridge JH, Agrawal YC. 1995. Glimpses of a wave boundary layer. *J. Geophys. Res.* 100:20729–44

Trowbridge JH, Elgar S. 2001. Turbulence measurements in the surf zone. *J. Phys. Oceanogr.* 31:2403–17

Trowbridge JH, Elgar S. 2003. Spatial scales of stress-carrying nearshore turbulence. *J. Phys. Oceanogr.* 33:1122–28

Trowbridge JH, Geyer WR, Bowen MM, Williams AJ. 1999. Near-bottom turbulence measurements in a partially mixed estuary: turbulent energy balance, velocity structure, and along-channel momentum balance. *J. Phys. Oceanogr.* 29:3056–72

Trowbridge JH, Lentz SJ. 1998. Dynamics of the bottom boundary layer on the northern California shelf. *J. Phys. Oceanogr.* 28:2075–93

Trowbridge JH, Madsen OS. 1984. Turbulent wave boundary layers 2. Second-order theory and mass transport. *J. Geophys. Res.* 89:7999–8007

Trowbridge JH, Scully ME, Sherwood CR. 2017. The cospectrum of stress-carrying turbulence in the presence of surface gravity waves. *J. Phys. Oceanogr.* In press. **https://doi.org/10.1175/JPO-D-17-0016.1**

Turner JS. 1973. *Buoyancy Effects in Fluids*. New York: Cambridge Univ. Press

Uchiyama Y, McWilliams JC, Shchepetkin AF. 2010. Wave-current interaction in an oceanic circulation model with a vortex-force formalism: application to the surf zone. *Ocean Model.* 34:16–35

van der Werf JJ, Doucette JS, O'Donoghue T, Ribberink JS. 2007. Detailed measurements of velocities and suspended sand concentrations over full-scale ripples in regular oscillatory flow. *J. Geophys. Res. Earth Surf.* 112:F02012

Veron F, Melville WK. 1999. Pulse-to-pulse coherent Doppler measurements of waves and turbulence. *J. Atmos. Ocean. Technol.* 16:1580–97

Warner JC, Geyer WR, Lerczak JA. 2004. Numerical modeling of an estuary: a comprehensive skill assessment. *J. Geophys. Res.* 110:C05001

Weatherly GL, Martin PJ. 1978. On the structure and dynamics of the oceanic bottom boundary layer. *J. Phys. Oceanogr.* 8:557–70

Wiberg PL, Harris CK. 1994. Ripple geometry in wave-dominated environments. *J. Geophys. Res.* 99:775–89

Wijesekera HW, Allen JS, Newberger PA. 2003. Modeling study of turbulent mixing over the continental shelf: comparison of turbulent closure schemes. *J. Geophys. Res.* 108:3103

Wilson GW, Hay AE, Bowen AJ. 2014. Observations of wave shear stress on a steep beach. *J. Geophys. Res.* 119:7827–39

Wyngaard JC. 1992. Atmospheric turbulence. *Annu. Rev. Fluid Mech.* 24:205–33

Yuan J, Madsen OS. 2015. Experimental and theoretical study of wave-current turbulent boundary layers. *J. Fluid Mech.* 765:480–523

Zhang GW, Gawarkiewicz GG, McGillicuddy DJ, Wilkin JL. 2011. Climatological mean circulation at the New England shelf break. *J. Phys. Oceanogr.* 41:1874–93

Zou Q, Bowen AJ, Hay AE. 2006. Vertical distribution of wave shear stress in variable water depth: theory and field observations. *J. Geophys. Res.* 111:C09032

ANNUAL REVIEWS
Connect With Our Experts
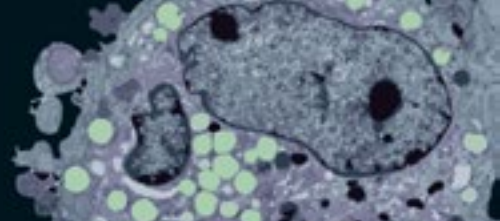
New From Annual Reviews:

Annual Review of Cancer Biology
cancerbio.annualreviews.org · Volume 1 · March 2017

ONLINE NOW!

Co-Editors: Tyler Jacks, *Massachusetts Institute of Technology*

Charles L. Sawyers, *Memorial Sloan Kettering Cancer Center*

The *Annual Review of Cancer Biology* reviews a range of subjects representing important and emerging areas in the field of cancer research. The *Annual Review of Cancer Biology* includes three broad themes: Cancer Cell Biology, Tumorigenesis and Cancer Progression, and Translational Cancer Science.

TABLE OF CONTENTS FOR VOLUME 1:

Contents

Errata

An online log of corrections to *Annual Review of Marine Science* articles may be found at
http://www.annualreviews.org/errata/marine